International Journal of Applied Earth Observation and Geoinformation 128 (2024) 103784

Contents lists available at ScienceDirect

International Journal of Applied Earth Observation and Geoinformation

journal homepage: www.elsevier.com/locate/jag

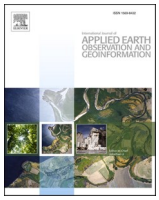

Mitigating underestimation of fire emissions from the Advanced Himawari Imager: A machine learning and multi-satellite ensemble approach

Yoojin Kang [a], Jungho Im [a,b,*]

[a] Department of Civil, Urban, Earth, and Environmental Engineering, Ulsan National Institute of Science and Technology, Ulsan, Republic of Korea
[b] Graduate School of Carbon Netrality, Ulsan National Institute of Science and Technology, Ulsan, Republic of Korea

ARTICLE INFO

Keywords:
Fire radiative power
Active fire
Machine learning
Biomass burning

ABSTRACT

The accurate estimation of biomass burning emissions has played a crucial role in air quality and climate forecast modeling. Satellite-based fire radiative power (FRP) has proven effective for calculating biomass burning emissions. However, FRP-based emission estimations in East Asia often rely on polar-orbiting satellites owing to the unstable performance of Japan Aerospace Exploration Agency Advanced Himawari Imager (JAXA AHI) from poor detection capability and unproper FRP retrieval method. To address this, we improve the FRP by machine learning based on mid-infrared (MIR) radiance method, leveraging the superior fire detection model developed in our previous study. In addition, we propose a multi-satellite distance-based weighted ensemble FRP estimation method. Compared to traditional MIR radiance methods, the machine learning-based FRP estimation model exhibited promising performance (correlation coefficient: 1, mean bias error: 0.2, mean absolute percentage error: 1.9%). The integration of machine learning-based FRP estimation and fire detection model dramatically mitigated the underestimation issues from the JAXA AHI. The machine learning-based FRP was combined with the Moderate Resolution Imaging Spectroradiometer FRP to create a multi-satellite ensemble FRP. Comparative assessments using the TROPOspheric Monitoring Instrument and conventional bottom-up method demonstrated that the proposed method produced reliable output. Furthermore, impact analysis revealed that missing peaks or underestimated burn scars could lead to fatally low emissions; however, the proposed method was relatively robust against missing data owing to its multi-satellite ensemble. By identifying potential FRP problems and their impact on emission estimations, this study provides valuable insights for FRP-based emission estimation studies.

1. Introduction

Wildfires have become a major global concern owing to their significant release of air pollutants and greenhouse gases into the atmosphere (Kim et al., 2017; Yarragunta et al., 2020). As fire emissions are crucial input sources for air quality and climate forecast modeling, long-standing efforts have been made to precisely estimate them (Jaffe et al., 2020; Liu et al., 2014; Pavlovic et al., 2016). Previously, the fire emission estimation method involved multiplying the burned area with the amount of available fuel, combustion efficiency, and emission factor (Zheng et al., 2021). However, this method has several potential uncertainties. For example, combustion efficiency varies with climate, topography, and vegetation conditions, making it difficult to obtain precise information on damaged area and available fuel (Olmedo et al., 2023). Another significant limitation is the time required to determine the burned area. Presently, the fire emission estimation method employs fire radiative power (FRP) from the satellite, which is the amount of instantaneous energy emitted by wildfires (Li et al., 2019). Unlike the former method, the FRP-based method offers the advantage of timely estimating fire emissions, particularly when utilizing geostationary satellites.

FRP can be calculated using the bi-spectral method, the mid-infrared temperature method, and the mid-infrared radiance method (Kim et al., 2017; Wooster et al., 2005). However, the bi-spectral method and the mid-infrared temperature method are not suitable for geostationary satellites stemming from the difficulty in setting proper neighboring windows due to the coarse spatial resolution. Although the mid-infrared (MIR) radiance method is the most suitable for computing FRPs from geostationary satellite data, it faces challenges in obtaining real-time MIR and broadband emissivity (Engel et al., 2022; Wooster et al., 2005).

Meanwhile, simplifying the computation steps by directly estimating the FRP from the brightness temperature can reduce the uncertainty

* Corresponding author.
E-mail address: ersgis@unist.ac.kr (J. Im).

https://doi.org/10.1016/j.jag.2024.103784
Received 3 October 2023; Received in revised form 22 February 2024; Accepted 17 March 2024
Available online 21 March 2024

factors and facilitate real-time calculation without considering emissivity. The direct modeling capabilities of machine learning have already been demonstrated by replacing complex radiative transfer models or omitting intermediate processes, leveraging its superiority in simulating nonlinear relationships between independent and dependent variables (Kang et al., 2022b; Yuan et al., 2020). Thus, machine learning application for FRP calculation can provide consistent FRP as well as the potential for machine learning to become one of the methods for generating FRP.

To refine geostationary satellite-based FRP, several adjustment methods have recently been proposed, including diurnal cycles and fusion with polar-orbiting satellite data (Andela et al., 2015; Zheng et al., 2021). The latter method effectively combines relatively accurate FRP from polar-orbiting satellites with the benefits of frequent FRP from geostationary satellites. It usually calibrates the geostationary satellite FRP to generate a Moderate Resolution Imaging Spectroradiometer (MODIS)-like FRP using the offset of MODIS because it is more reliable than geostationary satellite FRP (Li et al., 2018; Li et al., 2019). However, this largely depends on the assumption that the offset changes linearly and on the number and accuracy of MODIS observations. Accordingly, a more balanced ensemble method is expected to guarantee accuracy at other times when MODIS observations are unavailable.

The FRP retrieval necessitates prior active fire detection; however, the Japan Aerospace Exploration Agency Advanced Himawari Imager (JAXA AHI) has poor fire detection capability, resulting in underestimated overall FRP (Chatzopoulos-Vouzoglanis et al., 2023; Engel et al., 2022). If these underestimations accumulate over a large area for an extended period, they can pose a critical constraint on data usage. The problem caused by fire detection capability can be mitigated by using machine learning-based active fire detection models, which outperformed the JAXA AHI fire product. These detection models excel in East Asia, producing fire products that have similar spatial distribution and higher temporal frequency as those of MODIS and VIIRS active fire products (Kang et al., 2022; Kang et al., 2023).

Above simply identifying active fires, inaccuracies in detecting them within a specific spatial area can affect the accuracy of both the overall FRP and emissions. In addition, continuous detection may not be possible because of low detection capabilities or clouds. The effect will be amplified if the peak time FRP cannot be captured. Many situations can affect the emission calculations; however, a detailed analysis of this is rare at the fire cluster level. Thus, the impact analysis of various defect situations from FRP calculations will help identify the major limiting factors for emission estimation.

The objectives of this study were to: 1) improve AHI FRP using machine learning-based MIR radiance method and an enhanced fire detection model, 2) further enhance the FRP using a multi-satellite ensemble approach, 3) determine the impact of FRP defects on emission estimation for quantifying uncertainties, and 4) analyze uncertainties from combustion and emission factors at the fire cluster level.

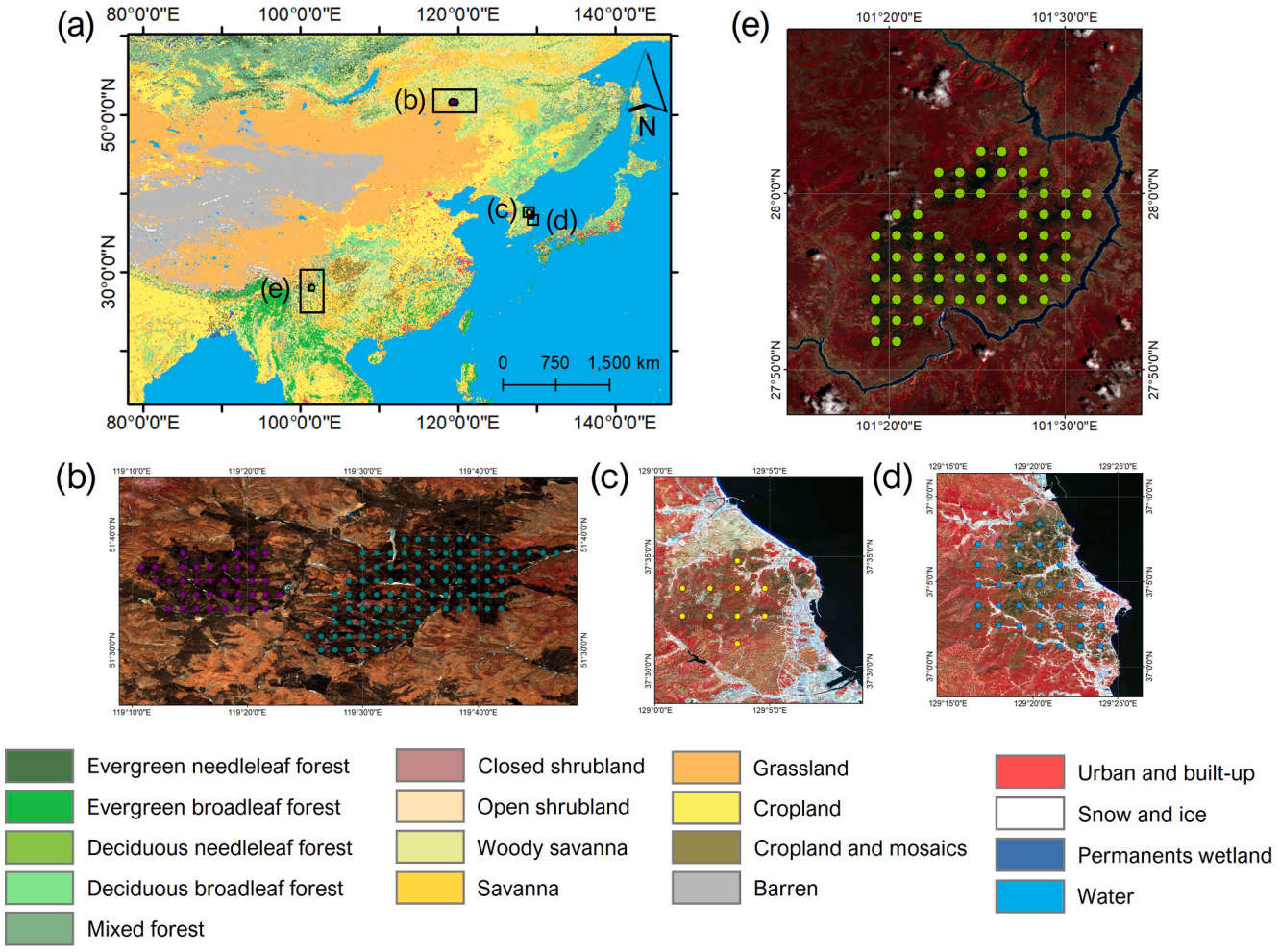

Fig. 1. (a) Map depicting the study area and the locations of the five cases of wildfire. The background image of land cover was obtained from MODIS. The specific sites of (b) cases 1 and 2, (c) case 3, (d) case 4, and (e) case 5 are described in zoomed images. In each zoomed image, the centers of Himawari-8 AHI pixels on the burn scar are marked with colored points. The background images in (b)–(e) include the Sentinel-2 false color composite (band 8, 4, and 3) after the fire.

2. Study area and data

2.1. Study area and cases

The target area of the present study included Southeast and East Asia, which has various vegetation types and witnesses frequent biomass burning. In the selected study area, we examined fire emissions from five long-lasting fires (cases 1–5) with identifiable fresh smoke (Fig. 1). The detection results for AHI, MODIS, visible infrared imaging radiometer (VIIRS), and the machine learning model for cases 1 and 2 were considerably different from each other (Kang et al., 2023). This made cases 1 and 2 ideal for analyzing emission changes based on fire detection results. Case 3 included a wildfire that burned an area of approximately 4,190 ha, whereas case 4—the largest wildfire occurred in South Korea—affected approximately 16,302 ha. Due to the simultaneous occurrence of these two wildfires, the surrounding area was significantly affected by air pollutants and greenhouse gases. Case 5 involved a wildfire in southern China, which primarily affected evergreen needleleaf forests and woody savannas. Detailed information is provided in Table S1.

2.2. Data

2.2.1. Himawari-8 AHI

The main input data for FRP estimation were obtained from the geostationary satellite Himawari-8 AHI, which has a fine temporal resolution of 10 min for 16 channels ranging from visible to thermal infrared (Zhang et al., 2023). The brightness temperatures of the 7th (3.85 μm) and 14th (11.2 μm) bands were used estimating FRP.

The JAXA AHI FRP was used as comparative model. It was calculated using the bi-spectral method (Engel et al., 2022). The FRPs for fires were detected at 10-minute intervals with a spatial resolution of 2 km. The JAXA AHI FRP has three reliability levels (low, normal, and high) and three quality flag levels (normal, saturated, and low confidence). Only high reliability and normal quality flag data were used in this study.

2.2.2. Polar-orbiting satellite-based FRP

The FRPs from MODIS and VIIRS were used for the ensemble FRP. MODIS (MCD14DL) and VIIRS (VNP14IMGTDL and VJ114IMGTDL) active fire data were downloaded from the National Aeronautics and Space Administration (NASA) FIRMS (https://earthdata.nasa.gov/active-fire-data), and the low confidence data were rejected (MODIS confidence < 30 % and VIIRS confidence $=$ low) (Giglio et al., 2018; Schroeder and Giglio, 2018). MODIS and VIIRS have contrasting advantages and disadvantages. The MODIS and VIIRS fire product have spatial resolutions of 1 km and 375 m, respectively. Although VIIRS has the advantage of detecting low FRP fires by utilizing its higher spatial resolution, its MIR band has a lower saturated temperature of 367 K. To address this issue, FRP is calculated using VIIRS 750 m M13 band (Schroeder and Giglio, 2018). In contrast, MODIS has a higher saturated temperature (500 K), but the lower limit of the FRP is approximately 10 MW because of its relatively coarse spatial resolution (Li et al., 2020a; Zheng et al., 2021).

2.2.3. Sentinel-5P TROPOspheric monitoring instrument vertical column density

The Sentinel-5P TROPOspheric Monitoring Instrument (TROPOMI) onboard the Copernicus Sentinel-5 Precursor satellite was used to compare fire emissions. In this study, nitrogen dioxide (NO_2) was used for evaluation, as suggested by Li et al., 2020b; because several values for primary emitted gases such as carbon monoxide and methane were missing (Li et al., 2020b) after filtering out low quality data (quality value < 0.5). TROPOMI provides data once a day, and the tropospheric NO_2 vertical column density (VCD) is provided with a 5.5 km $\times$ 3.5 km (7 km $\times$ 3.5 km before July 2021) spatial resolution (Park et al., 2022). Version 2.3.1 of the data product was downloaded from the NASA Earth data website (https://search.earthdata.nasa.gov/).

2.2.4. Auxiliary data

The MODIS normalized difference vegetation index (NDVI) data were used for calculating emissivity, a critical parameter for determining FRP through the MIR radiance method based on vegetation cover. The emission factor utilized for FRP calculations varies depending on the MODIS International Geosphere-Biosphere Program (IGBP) land cover class (Wiedinmyer et al., 2011). Thus, MYD13A2 and MCD12Q1 was downloaded from the NASA Earth Data (https://search.earthdata.nasa.gov/).

Burn scars are another element required to calculate emissions. As high-resolution official burn scar data were unavailable, high spatial resolution Sentinel-2 was used to obtain burn scars (Hu et al., 2021a; Lee et al., 2023). It has an optical imaging sensor (Multi-Spectral Instrument) with a 10 m spatial resolution in the visible channels (Hu et al., 2021a). Sentinel-2 L2A images captured in the regions of cases 1 and 2 on April 22, 2020, cases 3 and 4 on April 9, 2022, and case 5 on May 9, 2020, were used to extract the burn scars.

3. Methods

The methodology comprises four main steps: 1) FRP retrieval, 2) FRP ensemble, 3) emission estimation, and 4) comparative assessment and analysis (Fig. 2).

3.1. FRP retrieval

3.1.1. FRP modeling design

The FRP was calculated for active fires detected by the machine learning model (Kang et al., 2023). This model was developed using a convolutional neural network within the East Asia region and exhibited higher detection performance in unseen areas compared to the GK2A AMI and Himawari-8 AHI operational algorithms (Fig. 8 in Kang et al., 2023). Notably, the Himawari-8 AHI operational algorithm failed to detect the cases 1 and 2 used in this study, whereas the machine learning model successfully detected them, highlighting a significant distinction (Fig. 9 in Kang et al., 2023). For more detailed information about this model, please refer to Kang et al. (2023).

For FRP modeling, fire samples detected by the AHI were collected at 1 h intervals from 2017 to 2021. The MIR radiance method-derived AHI FRP served as a reference for the machine learning model. The MIR radiance method requires MIR band radiance, MIR emissivity, broadband emissivity, sensor coefficient, and the Stefan-Boltzmann constant. We followed the methodology from (Kim et al., 2017)) to retrieve FRP using the Communication Ocean and Meteorological Satellite geostationary satellite. In this methodology, MODIS NDVI was utilized to compute the fraction of vegetation cover, with subsequent determination of emissivity through the vegetation cover method (Valor and Caselles, 1996). The sensor coefficient of 3.11 was adopted, following the methodology presented by Kim and Lee (2016). A more detailed process of the MIR radiance method is described in Kim et al. (2017).

Although machine learning has a common advantage over simple formulas, the optimal technique differs depending on the research field or data. Besides, previous studies have not used machine learning to estimate FRP. Thus, three representative techniques, namely tree-based (Random Forest; RF), kernel-based (Support Vector Regression; SVR), and neural network-based (Artificial Neural Network; NN) machine learning techniques, were evaluated. Multiple linear regression (MLR) was used as a comparative model to examine the superiority of machine learning approaches over the simple model.

In contrast to traditional FRP retrieval methods, machine learning can solve complex relationships between input variables and FRP. Based on this, the MIR brightness temperature was included as an essential input variable and additional variables were considered for the machine learning-based FRP estimation model—the brightness temperature of

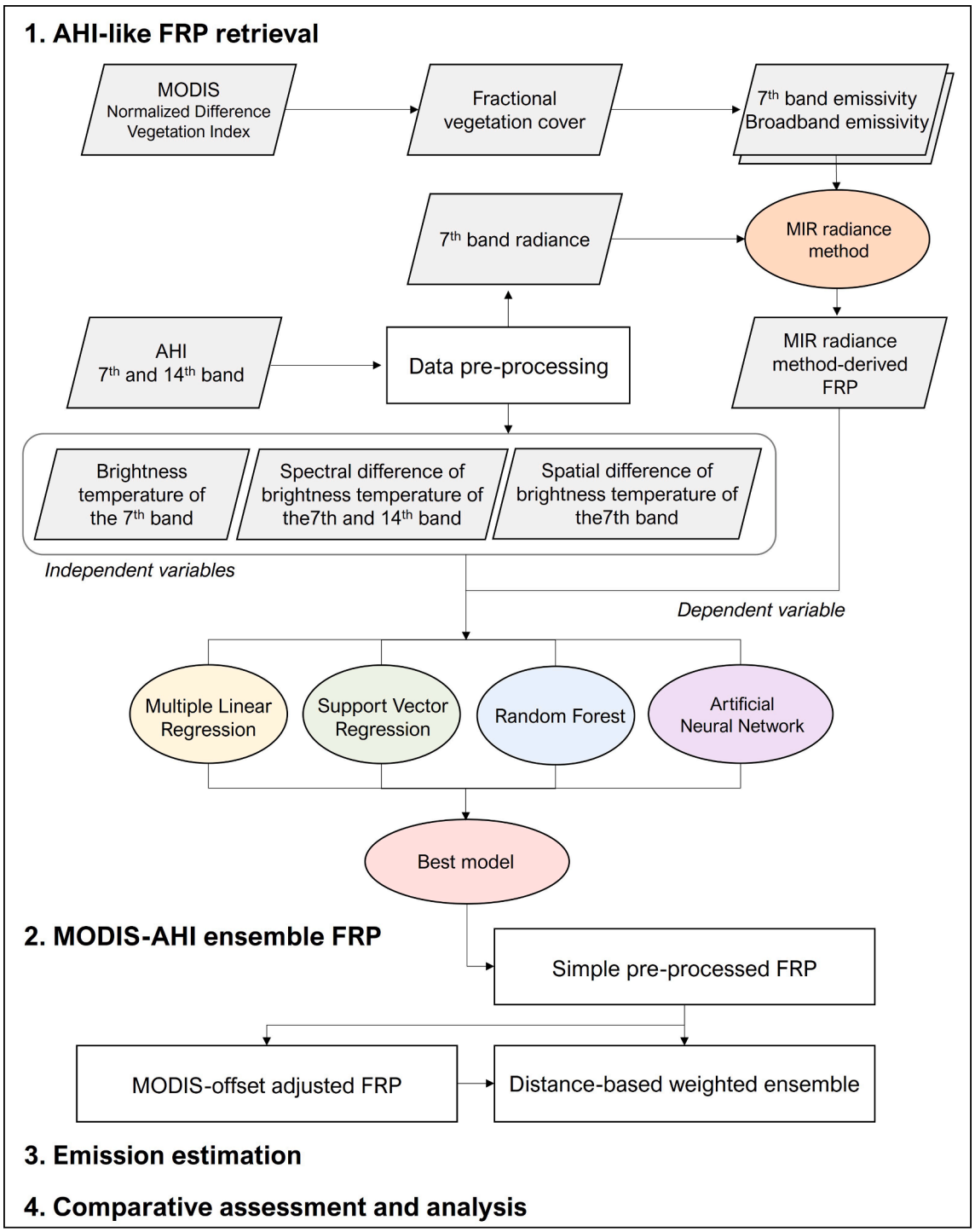

Fig. 2. Overall flow description of fire radiative power (FRP) and emission estimation process proposed in this study.

the 7th band (BT07), the spectral difference between the 7th and 14th bands (BT07-14), and the spatial difference between the center and neighboring pixels in the 7th band (SP07). BT07-14 represents the difference between the 7th and 14th channel brightness temperatures. SP07 was calculated as the brightness temperature difference between the center and the surrounding pixels in the 7th channel. The reason for using BT07-14 and SP07 was to consider the difference from the background temperature (Kang et al., 2022; Li et al., 2019).

3.1.2. Machine learning approaches

RF is an ensemble learner that uses several decision trees, random training data, and random input variables (Breiman, 2001) with an averaging approach to combine the results from various decision trees for regression (Cutler et al., 2007). The subset of training samples used to build the tree and subset of input variables used for each node of the tree were randomly chosen using the bootstrap aggregation process. In this study, the key parameters were set as num_tree = 1,000 and n_features = 'sqrt'.

SVR is a kernel-based technique that uses a kernel trick to convert low-dimensional data into high-dimensional data (Cho et al., 2020). For the regression tasks, an ideal hyperplane that could explain most of the data was found (Awad and Khanna, 2015). The most popular kernels are

the linear, polynomial, and radial basis functions. In this study, the radial basis function kernel was adopted because it exhibited the best performance among the three kernels.

NN consists of input, hidden, and output layers. Particularly, hidden layers are the core component, leveraging non-linear functions. The network is optimized through the iterative refinement of weights and biases, enabling it to learn complex relationships within the input and output layers(Hu et al., 2021b). In this study, the model was developed using three (16, 32, 16) hidden layers and the parameters max_iter = 1,000, learning_rate = 0.001, and activation_function = 'relu'.

3.2. FRP ensemble methods

3.2.1. Geostationary satellite-based diurnal cycle adjustment (GDC)

The diurnal cycle adjustment method was first developed using a polar-orbiting satellite (Vermote et al., 2009). The daily FRP was interpolated based on the assumption that the FRP has a diurnal cycle following a Gaussian distribution (Liu et al., 2015; Vermote et al., 2009). The FRP at a specific time (t) is calculated using Equation (1), where b, $\sigma, h, and FRP_{peak}$ were calculated using Equations (2)–(5), respectively. The parameter x is the Terra/Aqua FRP ratio, and ϵ is a term added to better simulate peak time for a specific location.

$$\mathrm{FRP}\,(\mathrm{t}) = FRP_{peak} \times (\mathrm{b} + e^{-\frac{(t-h)^2}{2\sigma^2}}) \tag{1}$$

$$\mathrm{b} = 0.86x^2 - 0.52x + 0.08 \tag{2}$$

$$\sigma = 3.89x + 1.03 \tag{3}$$

$$\mathrm{h}\,(\mathrm{FRP\ peak\ hour}) = -1.23x + 14.57 + \epsilon \tag{4}$$

$$FRP_{peak} = \frac{FRP_{Aquaday}}{\left[b + e^{-\frac{(13.5-h)^2}{2\sigma^2}}\right]} \tag{5}$$

Recently, diurnal cycle adjustments using geostationary satellites have also been proposed (Andela et al., 2015). It is also based on a Gaussian distribution; however, $\mathrm{FRP_{peak}}$ and $\mathrm{FRP_{base}}$ were extracted from the geostationary satellite FRP. The FRP at a specific time (t) was calculated using Equation (6).

$$FRP(t) = FRP_{base} + \left(FRP_{peak} - FRP_{base}\right) e^{-\frac{(h_t - h_{peak})^2}{2\sigma^2}}) \tag{6}$$

Here, FRP_{peak} is the daily maximum FRP, FRP_{base} corresponds to nighttime fire activity, h_t is the local solar time, and h_{peak} is the time when the FRP has a maximum value.

3.2.2. Modis-based linearly interpolated offset adjustment (MLO)

The linearly interpolated offset adjustment method corrects the geostationary satellite FRP to be closer to MODIS based on two assumptions: 1) MODIS can detect smaller and colder wildfires than the geostationary satellite, and 2) MODIS has consistent performance (Li et al., 2018; Li et al., 2019). The offset was calculated using the difference between the MODIS FRP and geostationary satellite FRP at the MODIS observation time. Without a MODIS FRP, the offset is 0, if one or two MODIS observations occur in a day, the offset is set to an average value, and it is linearly interpolated if MODIS is observed several times. Finally, the weighted average of the MODIS and calibrated geostationary satellite FRPs were used to calculate the fusion FRP.

3.2.3. Proposed ensemble FRP

The proposed ensemble method is divided into three steps: simple preprocessing, MLO, and a temporal distance-based weighted ensemble. Geostationary satellites frequently exhibit temporally sparse FRP because of cloud cover or sensor saturation. To address this, a 2 h moving average filter was used to remove noise and fill minor defects, followed by linear interpolation to fill the remaining missing values.

Next, calibration was performed at the fire cluster level. The FRP baseline was calibrated to ensure that the minimum values of the MODIS and preprocessed FRPs were equivalent. Following this, the offset with the preprocessed FRP from the MODIS FRP was calculated at the time of MODIS observation. The offset for the entire period was calculated using linear interpolation. This offset was then added to the pixel-level preprocessed FRP.

Finally, the temporal distance from the closest MODIS observation time is calculated for each observation time. The final FRP was calculated using a weighted ensemble of temporal distance-based weights (Equation (7), where the weight (w) is defined as temporal distance/2.

$$Ensemble\ FRP = \begin{cases} (1-w) \times MLO + w \times preprocessedFRP, temporaldistance < 12h \\ preprocessedFRP, otherwise. \end{cases} \tag{7}$$

3.3. *Emission* estimation

The emissions were calculated using a commonly used FRP-based emission estimation method (Equation (8). Emissions were calculated as the product of the fire radiative energy (FRE), conversion factor *CF*, and emission factor *EF*. The FRE and emissions for individual fires can be calculated if the FRP is integrated from the beginning to the end of the fire. *CF* is generally considered to have a constant value of 0.368 kg/MJ (±0.015 kg/MJ), as developed by (Wooster et al., 2005). *EF* varies depending on the fuel type and species, and the emission factor for each MODIS IGBP land cover class was used in this study (Akagi et al., 2011; Wiedinmyer et al., 2011).

$$\mathrm{E} = FRE \times CF \times EF = \int_{t1}^{t2} FRP\,dt \times CF \times EF \tag{8}$$

3.4. FRP evaluation

In this study, 10-fold cross-validation (CV) methods were adopted to train and validate an FRP estimation model. To evaluate the performance, three metrics were used: correlation coefficient (R), mean biased error (MBE), and mean absolute percent error (MAPE) (Equations (9)–(11):

$$R = \frac{\sum_{i=1}^{n}(x_i - \bar{x})(y_i - \bar{y})}{\sqrt{\sum_{i=1}^{n}(x_i - \bar{x})^2 \sum_{i=1}^{n}(y_i - \bar{y})^2}} \tag{9}$$

$$\mathrm{MBE} = \frac{\sum_{i=1}^{n}(y_i - x_i)}{\mathrm{n}} \tag{10}$$

$$\mathrm{MAPE} = \sum_{i=1}^{n} \frac{|y_i - x_i|}{y_i} \times \frac{100\%}{n} \tag{11}$$

where x_i and y_i are the predicted and observed data, respectively; $\bar{x}$ and $\bar{y}$ are the means of the predicted and observed data, respectively; and n is the number of observations.

3.5. Emission evaluation methods

Fire emissions were comparatively evaluated using the two approaches. First, TROPOMI observations were based on previous studies (Fu et al., 2022; Li et al., 2020b; Li et al., 2022). The NO_2 VCD above the smoke pixels were assumed to be indicators of fire emissions and were used to subtract the background NO_2 VCD from that of the smoke. The smoke pixels were first filtered to an area larger than mean and standard deviation, and then manually refined. The calculation steps were based on those described in a previous study (Li et al., 2022).

$$NO_2 = \sum_{i=1}^{n}[(\rho_{smoke}{}^{i} - \rho_{background}) \times A^i \times M] \quad (12)$$

where n is the total number of smoke pixels, $\rho_{smoke}{}^{i}$ and $\rho_{background}$ are the NO_2 VCD of the i^{th} smoke and background pixels (mol/m^2), respectively, A^i is the pixel area of the i^{th} pixel, and M is the molecular mass of NO_2 (46.0055 g/mol). The background pixels are non-smoke pixels in 41 × 41 windows centered around a smoke pixel.

Second, a conventional bottom-up method was used for comparative assessment. The CO_2 and CH_4 emissions for cases 3 and 4 calculated based on the Intergovernmental Panel on Climate Change (IPCC) 2006 guidelines. The calculation steps follow Equation (13):

$$Emission = A \times M \times C \times EF \quad (13)$$

where A is burned area (ha), M is the available fuel, C is the combustion efficiency (kg/ha), and EF is the emission factor (g/kg^{-1}). The available fuel was constructed using a tree and age map obtained from field observations in 2020. The combustion efficiency is determined by the burn severity, which is measured by the maximum likelihood classification of the burned area by Korea Forest Service. The emission factors followed the IPCC guidelines (Table S2).

3.6. Impact analysis

To quantify the impact and obtain insights into FRP and emission estimation from the fire detection capability, two types of impact analyses were conducted. Although the MODIS FRP has been regarded as the most reliable FRP product, VIIRS FRP has gradually been used to take advantage of its advanced detection capability (Zheng et al., 2021). As a result, VIIRS was used as an ensemble member instead of MODIS to determine whether it could improve the underestimated emissions owing to MODIS's detection capability.

Further impact analysis was performed using four scenarios depending on the detection coverage. Two of these were related to temporal detection coverage. The first scenario concerns the missing peak time FRP from a geostationary satellite. The effect on the emissions was investigated by removing the FRP data for 3 h before and after the highest FRP during the entire period. Second, interpolation was used to recover the missing values in the first scenario. The other two are related to spatial detection coverage. The change in total emissions was

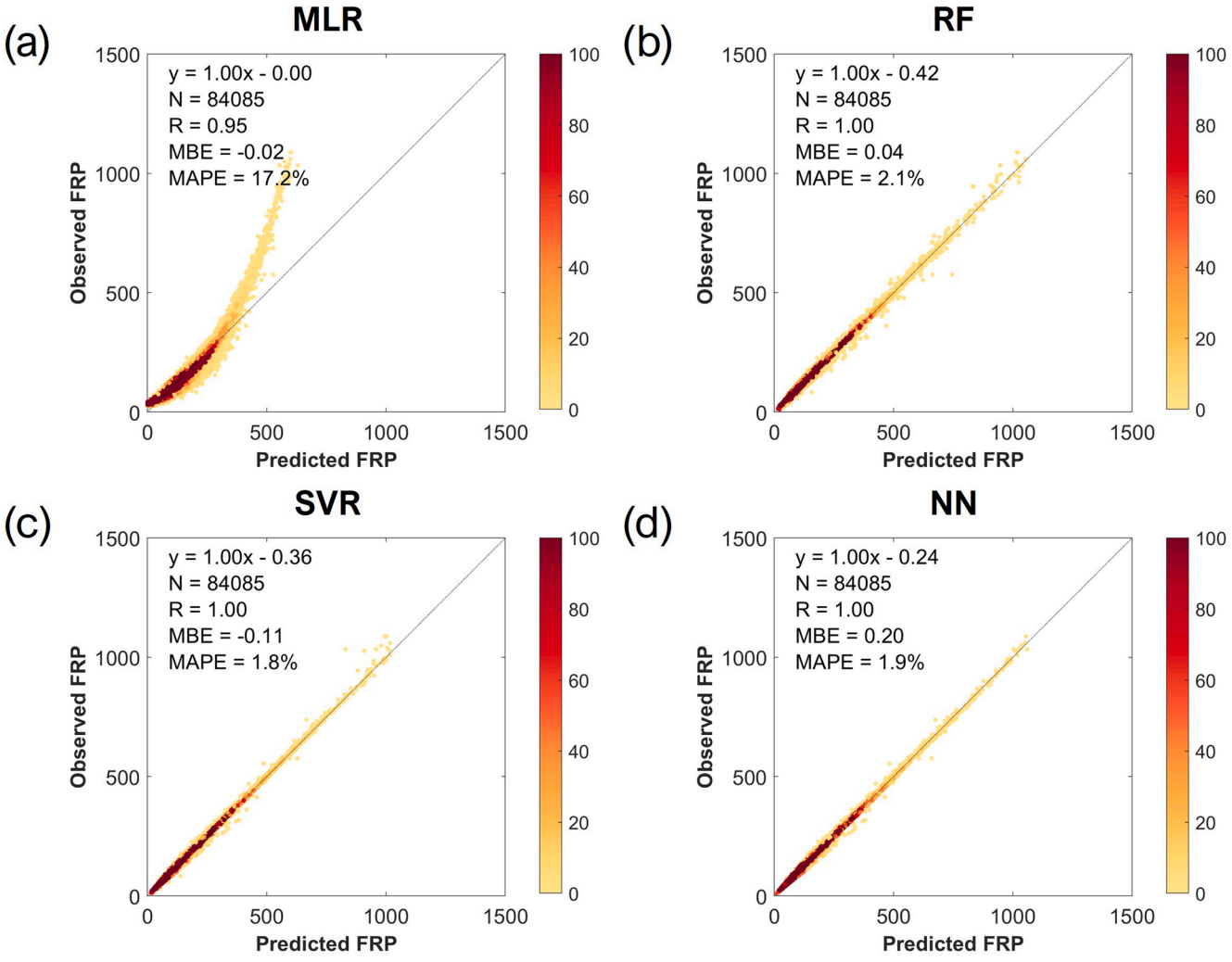

Fig. 3. Scatter plot results of 10-fold cross-validation for (a) multiple linear regression (MLR), (b) random forest (RF), (c) support vector regression (SVR), and (d) artificial neural network (NN). The color bar indicates the point density.

investigated by removing the edges of the burn scars to determine the impact of satellite misdetection. Finally, the impacts of overdetection and false alarms were examined using an area larger than that of the actual burn scar. The result of each scenario was evaluated using the percentage change (PC) from the ensemble model (Equation (14).

$$PC = 100 \times \frac{(y - x)}{x} \quad (14)$$

Where x and y are predicted and original ensemble models, respectively.

4. Results

4.1. FRP assessment

All models explained approximately 95–100 % of the variations in the MIR radiance method-derived FRP based on the R (Fig. 3). MLR exhibited a lower R and noticeably large MAPE than the machine learning-based models. These results indicate that machine learning guarantees much better performance in modeling FRP than MLR. Although the R and error values of all models were similar, the agreement at high FRP were different. NN had strong consistency at high FRP, whereas RF and SVR had more discrepancies. Therefore, NN was the optimal model, with the highest agreement with the MIR radiance method. The accuracy statistics of the NN were comparable to or better than the performance of AHI-based FRP compared with MODIS in previous studies (R = 0.878, MBE = –17.22, and MAPE = 19.96 % (Kim and Lee, 2016); R^2 = 0.98, and bias = 3 (Xu et al., 2017)). Therefore, we concluded that the NN can be substituted for the MIR radiance method for real time FRP modeling.

Cases 1 and 2 demonstrate the advantage of the machine learning-based active fire detection model in addressing the detection capability problem of JAXA AHI. The JAXA AHI wildfire detection algorithm failed to identify cases 1 and 2 and only partially detected cases 3, 4, and 5 for a limited period (Figure S1). In addition, JAXA AHI has a lower total FRP because it detects a smaller area of fire pixels than the machine learning model. The JAXA AHI detected only a few pixels with strong signals within the fire perimeter. In contrast, the machine learning model detected all five cases and provided a relatively continuous FRP.

Beyond the detection capability, the NN-based FRP simulated increasing and decreasing patterns well compared with the MODIS and VIIRS FRP (Fig. 4). Although the peak FRPs from NN in cases 3, 4, and 5 were somewhat lower than those from MODIS and VIIRS, the peak points matched quite well in cases 1 and 2. Therefore, we demonstrated that improved machine learning-based wildfire detection and FRP estimation models minimized the underestimation problem of the JAXA AHI FRP.

However, the NN-based FRP recorded a significantly lower total FRP than the MODIS and VIIRS FRPs at the peak time in case 5. This discrepancy occurred because the burning temperature during that period was extremely high, with a MODIS brightness temperature exceeding 450 K. However, the AHI sensor was saturated at 400 K, resulting in an underestimation of the FRP. This suggests that FRP may have been underestimated because of the comparatively lower saturation temperature of the AHI. However, the NN-based FRP is free from this problem because it is refined to the final FRP through an ensemble with the MODIS FRP (Figure S2). This highlighted the advantage of using ensemble FRP instead of relying on a single data source.

4.2. Intercomparison with TROPOMI-derived fire emissions

The maximum VCD pixel values are summarized in Table S3. The maximum NO_2 VCD values for cases 3 and 4 were approximately 10 times higher than those for cases 1 and 2, and the smoke caused by the fire could be clearly distinguished from the background (Fig. 5). Strong emissions were observed until 1–2 d after the wildfire, after which the effect almost disappeared.

A comparison of the TROPOMI-derived NO_2 and NO_2 emissions calculated from the GDC, MLO, and proposed ensemble (hereafter, Ensemble) methods is summarized in Table 1. GDC often underestimated emissions by 2–91 times compared with the other methods. The MLO and Ensemble methods yielded similar results. A good agreement between all the ways was observed in case 2 on April 10, 2020, and case 4 on March 4–5, 2022. These cases represent wildfires with strong NO_2 emissions, distinguishing the smoke from the background. The GDC, MLO, and Ensemble models produced reasonable results for emissions with strong signals.

Compared with the TROPOMI- and FRP-based NO_2 emissions integrated for 10 min, all three methods agreed well, except for case 5. The MLO and Ensemble methods exhibited a strong relationship for cases 1–4, with an R^2 of 0.96. Neither the TROPOMI- nor FRP-based emission estimation approaches can be considered true; therefore, no specific error analysis was conducted. However, the temporary emissions from both methods showed consistent variations, indicating the reliability of the proposed FRP-based emission estimation.

The mismatched NO_2 emissions over inherent uncertainties in the TROPOMI VCD and FRP can be attributed to several reasons. The coarse spatial resolution of the TROPOMI data posed a significant challenge in effectively detecting weak emissions (Li et al., 2022). Furthermore, the accuracy of smoke pixels selected using this simple method remained uncertain. In this study, fresh smoke was regarded as a conspicuous area in the TROPOMI images; therefore, it was estimated to be smaller than the actual smoke area. Moreover, although NO_2 is a highly reactive gas, we did not consider the varied emission factors that depend on the combustion phase and atmospheric effects in this study.

4.3. Emission intercomparison between FRP retrieval models

Overall, the ensemble method demonstrated reliability in emission estimation, as it closely matched the conventional bottom-up approach (Fig. 6). A common feature of the MLO and Ensemble emissions was their production of relatively higher emissions than the traditional bottom-up method. The overestimation by the FRP-based process may be because of 1) coarse spatial resolution of the AHI, 2) imprecise land cover type allocation, and 3) inaccurate pixel-by-pixel active fire periods. A detailed analysis of the first two reasons is provided in discussion. Finally, the model may over-detect the fire for longer than the actual period, owing to the pixel adjacency effect. In contrast, the conventional bottom-up method could have underestimated the overall emissions owing to the lower burn severity. In addition, the lower availability of fuel contributes to the underestimation of the overall emissions.

The FRP-based emission estimation method has few uncertainty factors and allows real-time calculations. However, missing data are unavoidable because they are based on satellite observations and accuracy (i.e., fire detection and FRP accuracy). In contrast, the conventional bottom-up method is not affected by missing satellite observations but requires acquiring numerous factors through direct measurements. Consequently, the traditional approach exhibits high uncertainty and is incompatible with real-time calculations. The FRP-based and burn area-based emission estimation methods are exhaustive solutions with different strengths and weaknesses.

5. Discussion

5.1. Impact analysis on emissions from various scenarios

A negative change occurred in the FRE when VIIRS was used as an ensemble member, compared with the MODIS-based ensemble results (Table 2). The number of VIIRS detections was slightly higher than that of MODIS, which was notable in case 3 (Fig. 7). This is supported by previous studies showing that VIIRS is more advantageous for detecting

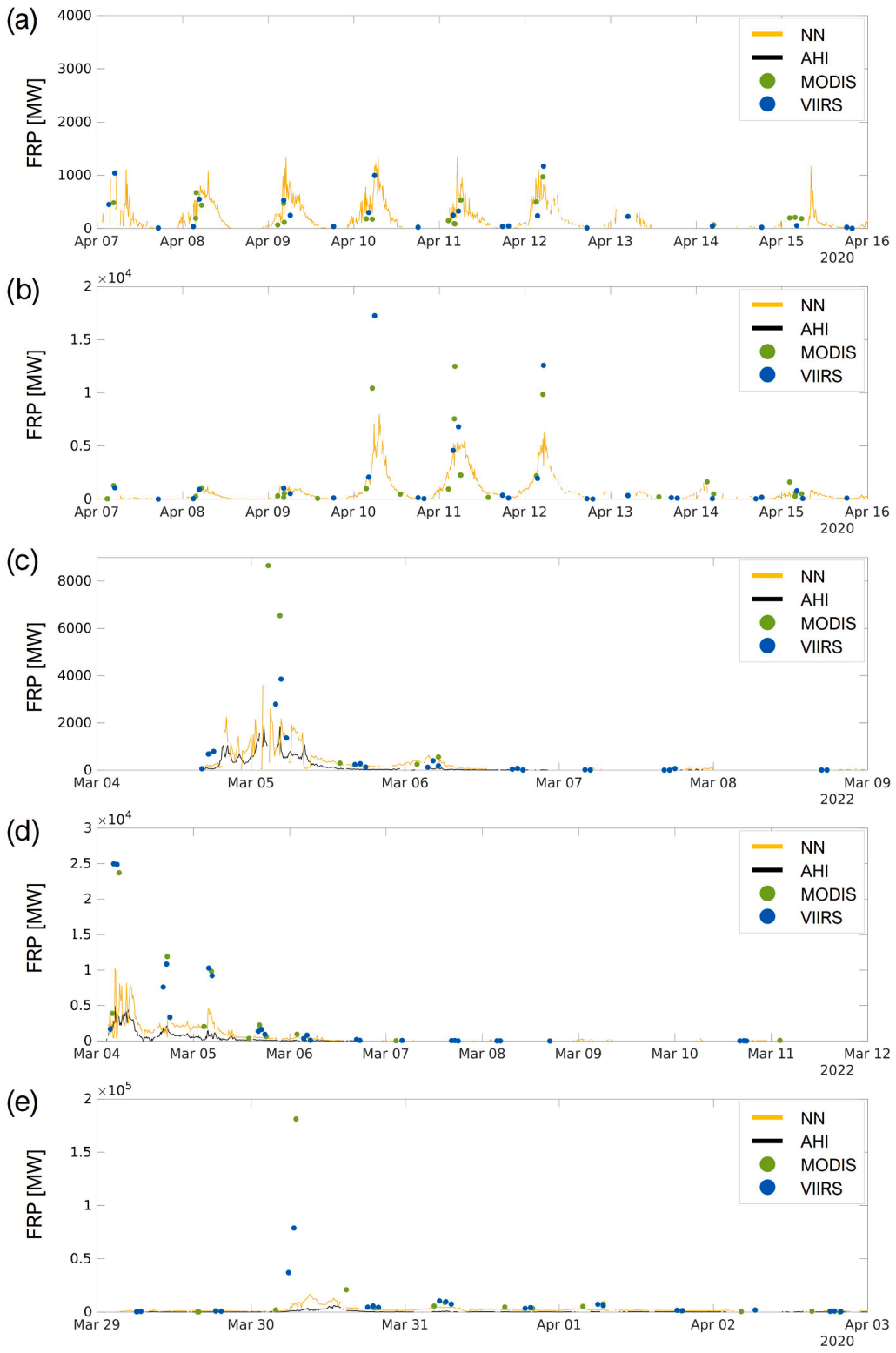

Fig. 4. The fire radiative power (FRP) time-series graph for (a) case 1, (b) case 2, (c) case 3, (d) case 4, and (e) case 5. The graph only shows the fire-concentrated period. The time interval between AHI and NN is 10 min. NN means the NN-based FRP.

weak wildfires and low FRP estimations (Li et al., 2020c). Moreover, a low FRP was simulated at the peak, resulting in a low overall FRE. MODIS had 370–395 K at its peak point, whereas VIIRS recorded a temperature of approximately 346 K. Even if MODIS does not detect weak wildfires, the overall FRE calculation will not be significantly affected if only the peak time FRP is properly provided. In conclusion, peak times must be properly detected when calculating emissions rather than continuously detecting wildfires. What cannot be determined is whether VIIRS underestimated the actual FRP or MODIS overestimated it because both satellites provided higher FRP at peak times than at other times. This indicates the need for more elaborate experiments to confirm the more accurate strategy.

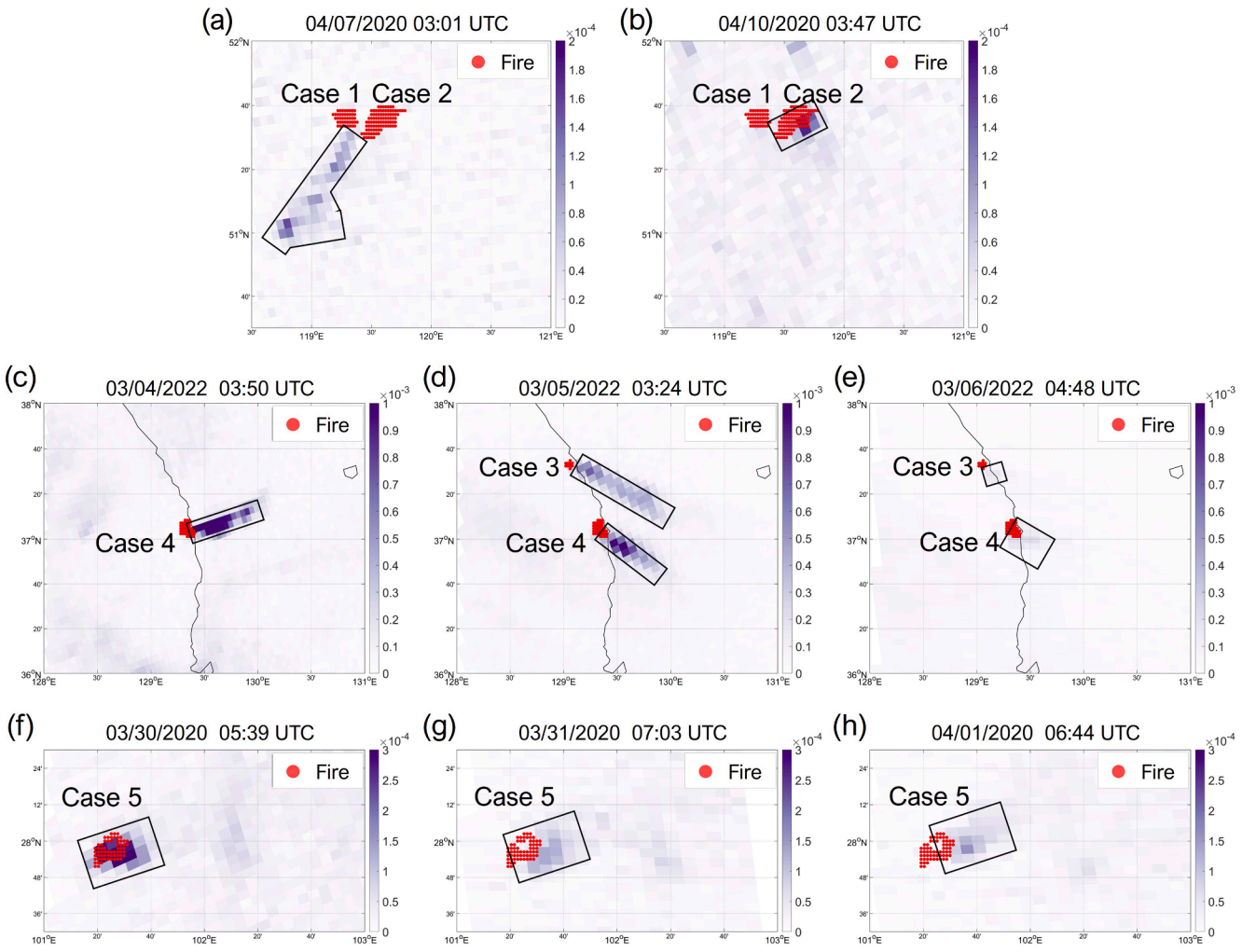

Fig. 5. The TROPOMI NO_2 vertical column density (VCD) in mol/m^2 of (a, b) cases 1 and 2, (c–e) cases 3 and 4, and (f–h) case 5. The red dots indicate the fire pixels. Black polygons roughly denote the areas affected by smoke. (For interpretation of the references to color in this figure legend, the reader is referred to the web version of this article.)

Table 1
NO_2 emissions (ton) derived from the TROPOMI, geostationary satellite-based diurnal cycle adjustment (GDC), MODIS-based linearly interpolated offset adjustment (MLO), and ensemble models.

Case	Date	Time (UTC)	NO_2 emission (ton)			
			TROPOMI	GDC	MLO	Ensemble
1	04/07/2020	04:40	3.22	0.10	2.94	2.94
2	04/10/2020	03:47	1.38	2.07	6.31	6.24
3	03/05/2022	03:24	11.22	3.30	20.95	19.99
3	03/06/2022	04:48	0.27	0.92	2.32	2.31
4	03/04/2022	03:50	21.69	13.98	31.29	31.18
4	03/05/2022	03:24	10.65	5.12	18.85	18.17
4	03/06/2022	04:48	1.19	0.60	3.69	3.12
5	03/30/2020	05:39	2.77	4.37	400.40	360.19
5	03/31/2020	07:03	1.82	6.50	39.50	36.95
5	04/01/2020	06:44	1.42	4.40	25.60	25.48

Similar to the polar-orbiting satellites, PC was the largest when the geostationary satellite did not capture the peak FRP (Fig. 8). However, if the missing values were filled in by interpolation, the error would have been significantly mitigated. Overall, the PC was below 9 % because it was partially compensated for by an ensemble with MODIS, even though geostationary FRP for peak time could not be obtained. Rather than relying on a single source, the multi-satellite ensemble model is useful in all cases for producing more stable emissions.

Negative PCs were observed if the FRP was calculated for an area smaller than the burn scar. The error was amplified if the pixels near the fire center were not detected. In contrast, PC was positive if an area larger than the burn scar was detected. However, the impact was much smaller than that of a smaller size. Because the pixels outside the burn scar have little effect from the fires, they contribute very little to the FRP. Therefore, misdetection is fatal to the emissions calculation, but over-detection or false alarms can be tolerated to some extent.

5.2. *Uncertainty analysis depending on the combustion factors*

The comparative assessment revealed that the FRP-based emissions differed between the TROPOMI-derived and conventional bottom-up methods. Previous studies have highlighted significant variations in emissions depending on the calculation method, with differences of up to approximately 18 times (Li et al., 2022). Therefore, we analyzed the reasons for the disparities in emissions, specifically focusing on

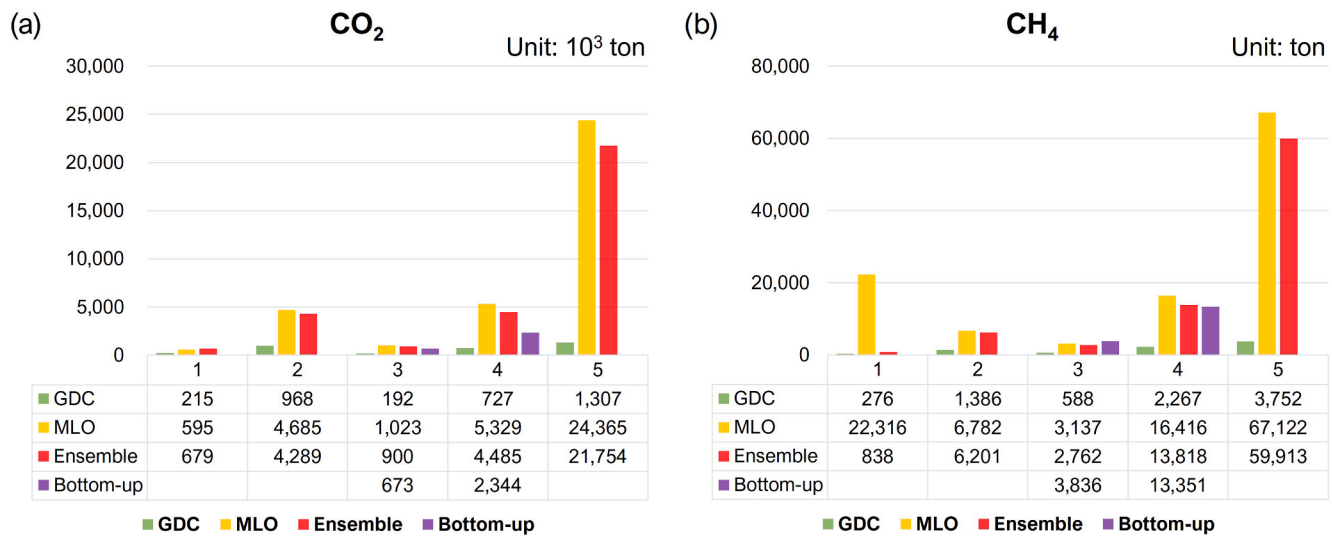

Fig. 6. Total emission estimation results of (a) CO_2 and (b) CH_4 for each fire case. The emission from the bottom-up is provided only for cases 3 and 4.

Table 2
Number of MODIS and VIIRS observations and related percentage change (PC with unit of %) for each fire case.

Case	The number of observations (MODIS/VIIRS)	PC
1	28/35	–31 %
2	36/39	–30 %
3	6/22	–192 %
4	13/26	–25 %
5	20/34	–33 %

combustion and emission factors.

This study adopted the widely used combustion factor of 0.368 that were refined following Wooster et al. (2005) (Li et al., 2022; McCarley et al., 2020). This implies the need to identify the underlying assumptions of the development of each factor and select the best-fit value for the study area (Table S4). Although closer to the bottom-up estimation as the combustion factor decreased, the FRP-based approach yielded significantly higher emissions (Figure S3). In contrast, considering the prevalence of pine forests in the study area, a higher *CF* is considered ideal. Thus, other factors may have caused the higher values from the proposed approach compared with the bottom-up approach.

Furthermore, the factors proposed in previous studies may not directly apply to the vegetation conditions in cases 3 and 4. This limitation arises because factors such as tree age and density, associated with fuel characteristics, affect combustion (Olmedo et al., 2023).

5.3. *Uncertainty analysis depending on the emission factors*

This study used emission factors based on the MODIS IGBP land cover class (Akagi et al., 2011). However, emission factors have been updated over time, and emission factors based on ecoregions have been proposed (Akagi et al., 2011; Andreae et al. 2015).

Assuming that the emission factor is accurate, disparities may arise from assigning the wrong emission factor owing to land cover misclassification or upscaling problems. For example, three cases could have been possible: 1) errors included in the land cover updates, 2) errors from the land cover classification, and 3) spatial resolution of the land cover data. Because the MODIS IGBP land cover class is provided annually around the middle of the succeeding year, the reflection of the actual land cover class is delayed. If the land cover for 2022 were the same as that in 2020, CO_2 would have been underestimated compared with the actual emissions, while CH_4 would have been overestimated (Table S5). When comparing the MODIS land cover with the high spatial resolution Environmental Systems Research Institute land cover data (Figure S4), some pixels were misclassified as savanna classes, even though South Korea did not have savanna areas. Finally, because this study was conducted at a spatial resolution of 2 km AHI, it may have included unburnt areas. Furthermore, although the land cover class was assigned as the representative class with the highest ratio per pixel, mixed land cover types could have existed within 2 km.

Considering the possibility that emission factors are inaccurate, different emission factors can be tested, including emission factors by ecoregion (Akagi et al., 2011; Adreae et al. 2019). However, it resulted in moderate differences. Utilizing the emission factor by ecoregion developed by Akagi resulted in variations of approximately 0.6 % (CO_2) and 18 % (CH_4) compared with that by the MODIS IGBP. Similarly, when employing the emission factor proposed by Andreae et al. (2019), the change ranged from –3.5 % (CO_2) to 8.8 % (CH_4).

6. Conclusion

The new trials conducted in this study have shown promising results. First, the FRP underestimation issue from JAXA AHI was effectively mitigated through the combination of machine learning-based active fire detection model and FRP estimation model. Second, the multi-satellite distance-based weighted ensemble FRP produced a more stable FRP than single-satellite techniques. If peaks were not detected or the burn scar was underestimated by geostationary satellite data, errors can be as high as –11.6 %. This could be prevented by a multi-satellite ensemble. Furthermore, the results of using VIIRS as an ensemble member suggested that it can serve as a viable alternative to MODIS FRP.

The impact analysis suggests that misdetection rather than false alarm is fatal to FRP-based emission estimation and emphasizes the need for sensitive active fire detection and FRP retrieval algorithms. The uncertainty analysis is expected to help understand the reason for the difference in total emissions from different satellites and methods (burned area-based or FRP-based). This research provided a basis for FRP-based emission at the fire cluster level, which deserves further investigation for generalized findings.

CRediT authorship contribution statement

Yoojin Kang: Conceptualization, Formal analysis, Investigation, Methodology, Validation, Writing – original draft. **Jungho Im:** Conceptualization, Methodology, Supervision, Writing – review & editing.

Fig. 7. Ensemble fire radiative power (FRP) time-series graph for case 3 with (a) MODIS and (b) VIIRS as an ensemble member. The time interval of points is 10 min.

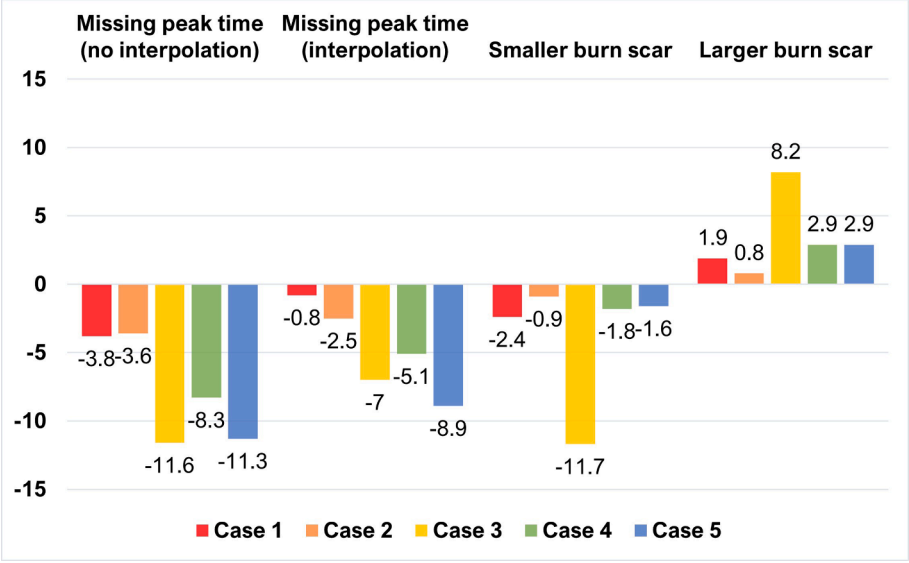

Fig. 8. Percentage changes (PCs with a unit of % per hour or % per pixel) of four scenarios for each fire case.

Declaration of competing interest

The authors declare that they have no known competing financial interests or personal relationships that could have appeared to influence the work reported in this paper.

Data availability

Data will be made available on request.

Acknowledgement

This work was supported by Korea Environment Industry & Technology Institute(KEITI) through Project for developing an observation-based GHG emissions geospatial information map, funded by Korea Ministry of Environment(MOE) (RS-2023-00232066).

Appendix A. Supplementary material

Supplementary data to this article can be found online at https://doi.org/10.1016/j.jag.2024.103784.

References

Akagi, S., Yokelson, R.J., Wiedinmyer, C., Alvarado, M., Reid, J., Karl, T., Crounse, J., Wennberg, P., 2011. Emission factors for open and domestic biomass burning for use in atmospheric models. Atmos. Chem. Phys. 11, 4039–4072.

Andela, N., Kaiser, J.W., van der Werf, G.R., Wooster, M.J., 2015. New fire diurnal cycle characterizations to improve fire radiative energy assessments made from MODIS observations. Atmos. Chem. Phys. 15, 8831–8846.

Awad, M., Khanna, R., 2015. Efficient learning machines: theories, concepts, and applications for engineers and system designers. Springer nature.

Breiman, L., 2001. Random forests. Mach. Learn. 45, 5–32.

Chatzopoulos-Vouzoglanis, K., Reinke, K.J., Soto-Berelov, M., Jones, S.D., 2023. One year of near-continuous fire monitoring on a continental scale: Comparing fire radiative power from polar-orbiting and geostationary observations. Int. J. Appl. Earth Obs. Geoinf. 117, 103214.

Cho, D., Yoo, C., Im, J., Lee, Y., Lee, J., 2020. Improvement of spatial interpolation accuracy of daily maximum air temperature in urban areas using a stacking ensemble technique. Gisci. Remote Sens. 57, 633–649.

Cutler, D.R., Edwards Jr, T.C., Beard, K.H., Cutler, A., Hess, K.T., Gibson, J., Lawler, J.J., 2007. Random forests for classification in ecology. Ecology 88, 2783–2792.

Engel, C.B., Jones, S.D., Reinke, K.J., 2022. Fire radiative power (FRP) values for biogeographical region and individual Geostationary HHMMSS threshold (BRIGHT) hotspots derived from the advanced Himawari imager (AHI). Remote Sens. (Basel) 14, 2540.

Fu, Y., Li, R., Hu, J., Wang, Y., Duan, J., 2022. Investigating the impacts of satellite fire observation accuracy on the top-down nitrogen oxides emission estimation in northeastern Asia. Environ. Int. 169, 107498.

Giglio, L., Schroeder, W., Hall, J., Justice, C., MODIS Collection 6 Active Fire Product User's Guide Revision B. 2018. NASA.

Hu, X., Ban, Y., Nascetti, A., 2021a. Sentinel-2 MSI data for active fire detection in major fire-prone biomes: a multi-criteria approach. Int. J. Appl. Earth Obs. Geoinf. 101, 102347.

Hu, X., Zhang, P., Zhang, Q., Wang, J., 2021b. Improving wetland cover classification using artificial neural networks with ensemble techniques. Giscience & Remote Sensing 58, 603–623.

Jaffe, D.A., O'Neill, S.M., Larkin, N.K., Holder, A.L., Peterson, D.L., Halofsky, J.E., Rappold, A.G., 2020. Wildfire and prescribed burning impacts on air quality in the United States. J. Air Waste Manag. Assoc. 70, 583–615.

Kang, Y., Jang, E., Im, J., Kwon, C., 2022. A deep learning model using geostationary satellite data for forest fire detection with reduced detection latency. Giscience & Remote Sensing 59, 2019–2035.

Kang, Y., Sung, T., Im, J., 2023. Toward an adaptable deep-learning model for satellite-based wildfire monitoring with consideration of environmental conditions. Remote Sens. Environ. 298, 113814.

Kim, D., Lee, Y., 2016. Retrieval of Fire Radiative Power from Himawari-8 Satellite Data Using the Mid-Infrared Radiance Method. J. Korean Soc. Geospatial Inf. Sci. 24, 105-113.

Kim, D., Cho, J., Hong, S., Lee, H., Won, M., Byun, S., Park, K., Lee, Y.-W., 2017. First retrieval of fire radiative power from COMS data using the mid-infrared radiance method. Remote Sens. Lett. 8, 116–125.

Lee, K., Kim, B., Park, S., 2023. Evaluating the potential of burn severity mapping and transferability of copernicus EMS data using Sentinel-2 imagery and machine learning approaches. Giscience & Remote Sensing 60, 2192157.

Li, F., Zhang, X., Kondragunta, S., Roy, D.P., 2018. Investigation of the fire radiative energy biomass combustion coefficient: a Comparison of Polar and Geostationary satellite retrievals over the conterminous United States. J. Geophys. Res. Biogeo. 123, 722–739.

Li, F., Zhang, X., Roy, D.P., Kondragunta, S., 2019. Estimation of biomass-burning emissions by fusing the fire radiative power retrievals from polar-orbiting and geostationary satellites across the conterminous United States. Atmos. Environ. 211, 274–287.

Li, F., Zhang, X., Kondragunta, S., 2020a. Biomass burning in Africa: an investigation of fire radiative power missed by MODIS using the 375 m VIIRS active fire product. Remote Sens. (Basel) 12, 1561.

Li, F., Zhang, X., Kondragunta, S., Lu, X., 2020b. An evaluation of advanced baseline imager fire radiative power based wildfire emissions using carbon monoxide observed by the tropospheric monitoring instrument across the conterminous United States. Environ. Res. Lett. 15, 094049.

Li, F., Zhang, X., Kondragunta, S., Schmidt, C.C., Holmes, C.D., 2020c. A preliminary evaluation of GOES-16 active fire product using Landsat-8 and VIIRS active fire data, and ground-based prescribed fire records. Remote Sens. Environ. 237, 111600.

Li, F., Zhang, X., Kondragunta, S., Lu, X., Csiszar, I., Schmidt, C.C., 2022. Hourly biomass burning emissions product from blended geostationary and polar-orbiting satellites for air quality forecasting applications. Remote Sens. Environ. 281, 113237.

Liu, Y., Goodrick, S., Heilman, W., 2014. Wildland fire emissions, carbon, and climate: wildfire–climate interactions. For. Ecol. Manage. 317, 80–96.

Liu, M., Song, Y., Yao, H., Kang, Y., Li, M., Huang, X., Hu, M., 2015. Estimating emissions from agricultural fires in the North China plain based on MODIS fire radiative power. Atmos. Environ. 112, 326–334.

Olmedo, G.F., Gilabert, H., Bown, H., Sanhueza, R., Silva, P., Jorquera-Stuardo, C., Sierra, F., 2023. Improving the Combustion Factor to Estimate GHG Emissions Associated with Fire in Pinus radiata and Eucalyptus spp. Plantations in Chile, Forests.

Park, J.-U., Park, J.-S., Diaz, D.S., Gebetsberger, M., Müller, M., Shalaby, L., Tiefengraber, M., Kim, H.-J., Park, S.S., Song, C.-K., Kim, S.-W., 2022. Spatiotemporal inhomogeneity of total column NO2 in a polluted urban area inferred from TROPOMI and Pandora intercomparisons. Gisci. Remote Sens. 59, 354–373.

Pavlovic, R., Chen, J., Anderson, K., Moran, M.D., Beaulieu, P.-A., Davignon, D., Cousineau, S., 2016. The FireWork air quality forecast system with near-real-time biomass burning emissions: recent developments and evaluation of performance for the 2015 north American wildfire season. J. Air Waste Manag. Assoc. 66, 819–841.

Schroeder, W., Giglio, L., 2018. NASA VIIRS land science investigator processing system (SIPS) visible Infrared imaging radiometer suite (VIIRS) 375 m & 750 m active fire products: product user's guide version 1.4. Product User's Guide Version 1, 23.

Valor, E., Caselles, V., 1996. Mapping land surface emissivity from NDVI: application to european, african, and south American areas. Remote Sens. Environ. 57, 167–184.

Vermote, E., Ellicott, E., Dubovik, O., Lapyonok, T., Chin, M., Giglio, L., Roberts, G.J., 2009. An approach to estimate global biomass burning emissions of organic and black carbon from MODIS fire radiative power. J. Geophys. Res. Atmos. 114.

Wiedinmyer, C., Akagi, S.K., Yokelson, R.J., Emmons, L.K., Al-Saadi, J.A., Orlando, J.J., Soja, A.J., 2011. The fire INventory from NCAR (FINN): a high resolution global model to estimate the emissions from open burning. Geosci. Model Dev. 4, 625–641.

Wooster, M.J., Roberts, G., Perry, G.L.W., Kaufman, Y.J., 2005. Retrieval of biomass combustion rates and totals from fire radiative power observations: FRP derivation and calibration relationships between biomass consumption and fire radiative energy release. J. Geophys. Res. Atmos. 110.

Xu, W., Wooster, M.J., Kaneko, T., He, J., Zhang, T., Fisher, D., 2017. Major advances in geostationary fire radiative power (FRP) retrieval over Asia and Australia stemming from use of Himarawi-8 AHI. Remote Sens. Environ. 193, 138–149.

Yarragunta, Y., Srivastava, S., Mitra, D., Chandola, H.C., 2020. Influence of forest fire episodes on the distribution of gaseous air pollutants over Uttarakhand, India. Gisci. Remote Sens. 57, 190–206.

Zhang, Y., Wang, W., He, J., Jin, Z., Wang, N., 2023. Spatially continuous mapping of hourly ground ozone levels assisted by Himawari-8 short wave radiation products. Gisci. Remote Sens. 60, 2174280.

Zheng, Y., Liu, J., Jian, H., Fan, X., Yan, F., 2021. Fire diurnal cycle derived from a combination of the Himawari-8 and VIIRS satellites to improve fire emission assessments in Southeast Australia. Remote Sens. 13, 2852.